Journal of Power Sources 413 (2019) 459–466

Contents lists available at ScienceDirect

Journal of Power Sources

journal homepage: www.elsevier.com/locate/jpowsour

High-efficiency perovskite solar cells based on self-assembly n-doped fullerene derivative with excellent thermal stability

Xiaotao Liu[a,1], Pengwei Li[b,1], Yiqiang Zhang[a,*,1], Xiaotian Hu[b], Yanyan Duan[a], Fengyu Li[b,c], Dan Li[c], Guosheng Shao[a], Yanlin Song[b,**]

[a] State Centre for International Cooperation on Designer Low-Carbon and Environmental Material (SCICDLCEM), School of Materials Science and Engineering, Zhengzhou University, Zhengzhou, 450001, PR China
[b] Key Laboratory of Green Printing, Institute of Chemistry, Chinese Academy of Sciences (ICCAS), Beijing Engineering Research Centre of Nanomaterials for Green Printing Technology, Beijing National Laboratory for Molecular Sciences (BNLMS), Beijing, 10090, PR China
[c] College of Chemistry and Materials Science, Jinan University, Guanzhou, 510632, PR China

HIGHLIGHTS

- Deposited doped PTEG-1 is not required thermally annealing.
- The doped PTEG-1 self-assembled into stable layered structure.
- $CH_3NH_3PbI_3$-based n-i-p cells exhibit a PCE of 18.5%.
- Devices sustain 85% of initial efficiency after 1000 h under 60 °C.

GRAPHICAL ABSTRACT

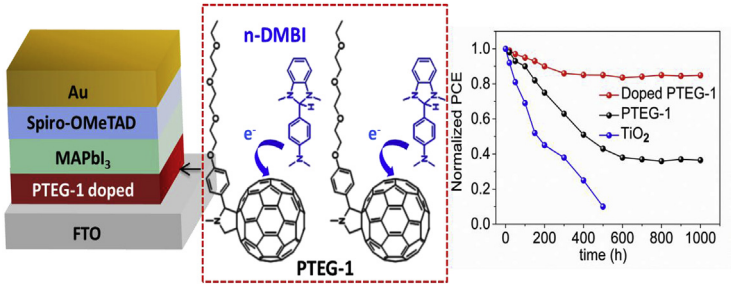

ARTICLE INFO

Keywords:
Thermal stability
Perovskite solar cells
n-type doping
Fullerene derivatives
Low temperature process

ABSTRACT

Perovskite solar cells are promising photovoltaic devices with high efficiency beyond 23%, but thermal instability is one of the key obstacles for the commercialization. To prolong thermal stability, (4-(1,3-dimethyl-2,3-dihydro-1H-benzoimidazol-2-yl) phenyl)dimethylamine is doped into a state-of-the-art fullerene derivative with a hydrophilic triethylene glycol type side chain as electron transport layer in planar perovskite cells with low-temperature process (< 100 °C). The addition of dopant in electron transport layer results in stable layered structure. We observe that the increase of electron transport layer conductivity and optimized reduction of work function facilitate charge extraction and improve the energy level alignment. As a result, $CH_3NH_3PbI_3$-based n-i-p perovskite cells with doped electron transport layer exhibit a hysteresis-free power conversion efficiency of 18.5%, outperforming the ones based on pristine electron transport layer (16.2%) or the other fullerene derivatives. Strikingly, the corresponding unsealed devices in air show long-term thermal stability. Devices sustain 85% of their initial efficiency after 1000 h storage under 60 °C. Our work bodes well for the dawn of commercialization of perovskite devices, providing the chance for the exploration of such high-efficiency devices with long-term thermal stability on flexible substrates.

* Corresponding author.
** Corresponding author.
E-mail addresses: yqzhang@zzu.edu.cn (Y. Zhang), ylsong@iccas.ac.cn (Y. Song).
[1] These authors contributed equally to this work.

https://doi.org/10.1016/j.jpowsour.2018.12.066
Received 22 August 2018; Received in revised form 7 December 2018; Accepted 23 December 2018
0378-7753/

1. Introduction

Organic-inorganic hybrid perovskite solar cells (PSCs) have sparked a great interest in both academia and industry, thanks to their long electron-hole diffusion lengths, tunable band gap, low recombination rate, solution process capability, and high performance [1–3]. Within a few years, the power conversion efficiency (PCE) of PSCs has been rapidly grown from 3.8% to 23%, mainly employing n-i-p as device structure and mesoporous-TiO_2 as electron transport layer (ETL) [4,5]. Despite the rapid progress in PCE of PSCs, UV-light photocatalysis and thermal degradation of TiO_2 are still the main challenges before PSCs become a real substitute for silicon solar cells [6,7]. Some alternative inorganic materials with inert photocatalysis capability, such as ZnO and SnO_2, have been applied as ETL in photo-stable PCSs [8,9]. Moreover, most stability investigations on PSCs so far were conducted under room temperature [10,11]. Thermal stability studies at 60 °C are less reported due to the poor performance of PSCs. Therefore, it is pivotal to explore novel electron transport materials with inert photosensitivity, high thermal stability and high electron mobility.

As excellent n-type organic semiconductors for optoelectronic devices, fullerene derivatives exhibit efficient electron mobility and strong thermal/moisture resistance [12–14]. PCBM, one of the main fullerene derivatives, is commonly used in planar p-i-n PSCs due to its excellent stability and negligible hysteresis [15,16]. Unfortunately, the PCE of PSCs based on PCBM relatively lagged compared to that of the TiO_2-based devices, owing to the insufficient electrical conductivity and high interfacial recombination rate of PCBM [17,18]. Doping strategy has been developed as an effective way to improve conductivity of PCBM [19–21]. Specifically, to reduce interfacial charge recombination between PCBM and electrode, we have demonstrated that the insertion of polyethyleneimine (PEI) interlayer between PCBM and electrode can improve the device stability [22]. In 2016, an alternative fullerene derivative with a hydrophilic triethylene glycol type side chain (PTEG-1) was used as ETL in planar PSCs. The devices using PTEG-1 as the ETL showed a higher PCE (15.71%) than PCBM-based PSCs [23]. Thus, it is necessary to further exploit high-mobility fullerene derivative ETL for PSCs. Additionally, the thermal stability of fullerene-derivative-based PSCs at 60 °C under long time operation (> 1000 h) is also crucial for PSCs commercialization.

In this work, we investigate the doping effect of n-DMBI in PTEG-1 host material, aiming to achieve high-performance PSCs with strong thermal stability. n-DMBI, as a n-type organic thermoelectrics, shows intrinsic high conductivity and thermal stability [24,25]. Employing the n–doped PTEG-1 ETL which is not required thermally annealed after solution deposition, we obtained a PCE of 18.5% under standard AM 1.5G solar illumination for PSCs. The introduction of n-DMBI in the PTEG-1 layer led to increase its conductivity, bringing to higher short circuit current density (J_{SC}) = 22.85 mA/cm^2 and fill factor (FF) = 78%, corresponding to an open-circuit voltage (V_{OC}) of 1.04 V. Interestingly, the work function of the ETL layers gradually decreases with increasing n-DMBI doping concentration. The decreased work function demonstrates the upward movement of the Fermi level (E_F) in the bandgap and an increased carrier density by introducing more dopant. The n-DMBI doping can increase electrical conductivity, electron mobility, and charge extraction ability in the ETL layer. Furthermore, the doped PTEG-1 cells kept 85% of the initial PCE after over 40-days storage at 60 °C with the humidity of 20%. These results indicate that the addition of n-DMBI dopant into n–i–p planar PSCs is an effective method for improving device efficiency and thermal stability.

2. Experimental section

2.1. Materials

A majority of materials were purchased from Alfa-Aesar without further purification. PETG-1 was synthesized and purified by ourselves. PbI_2 and n-DMBI was obtained from Xi'an Polymer Light Technology Corp. and Sigma Aldrich, respectively. Methylammonium iodide (MAI) was synthesized by the reaction of 24 mL CH_3NH_2 (33 wt% in absolute ethanol, Alfa) and 30 mL HI (57 wt% in water, Alfa) at 0 °C stirring for 2 h. The precipitate of MAI was then evaporated at 55 °C for 1 h. Then, the MAI powder was washed three times with diethyl ether by stirring the solution for oven 30 min before being dried in a vacuum at 60 °C for 48 h, finally stored in N_2 atmosphere. The $CH_3NH_3PbI_3$ precursor solution was fabricated by following the method, where 1152 mg of PbI_2, 398 mg of MAI, and 400 μL of DMSO were mixed with 1600 μL of DMF. Then, the solution was stirred for oven 12 h at 65 °C in a N_2-filled glovebox.

2.2. Fabrication of perovskite solar cells

The perovskite solar cells were fabricated on fluorine-doped tin oxide (FTO) coated glass (8 Ω/sq) with the following device configuration: FTO/ETL/$CH_3NH_3PbI_3$/Spiro-OMeTAD/Au. The FTO glass was cleaned by sequential ultrasonic treatment cleaning in de-ionized water, acetone, ethyl alcohol and isopropyl alcohol for 15 min each orderly, and then dried at room temperature. After drying, the substrates were treated within a UV-ozone chamber for 15 min to remove the organic residues. Firstly, thick electron extraction layer (50 nm) was spin-coated on top of the FTO glass from solutions of PTEG-1 and PTEG-1 doped with a variable ratio, respectively. Secondly, for the deposition of perovskite film, the as-prepared fresh $CH_3NH_3PbI_3$ precursor solution was spin-coated on the PTEG-1 film, and then annealed at 100 °C for 10 min. Specifically, the $CH_3NH_3PbI_3$ precursor solution was dropped to cover the active device area, and immediately the spin-coating recipe was initiated via two consecutive steps of 1500 r.p.m. for 15 s and then 4000 rpm for 20 s. In the last 5 s, 300 μL toluene of was dropped at the center of this substrate to drive mixed DMSO/DMF solvent away. Thirdly, the HTL was spin-coated on the perovskite layer by 3000 r.p.m. for 30 s. The precursor solution was prepared by dissolving 144.6 mg Spiro-OMeTAD, 57.6 μL 4-tert-butylpyridine, and 35 μL bis(trifluoromethane) sulfonamide lithium salt (Li-TFSI) solution (LiTFSI, 520 mg/mL in acetonitrile) in 2 mL chlorobenzene. Finally, 80 nm of Au was thermal deposited as a counter electrode through a shadow mask using a Trovato thermal evaporator. The active device area was 0.04 cm^2.

2.3. Instruments

The current density-voltage (J–V) characteristics were obtained using a Keithley 2400 source meter and a collimated Xenon lamp (300 W, Newport) calibrated with the light intensity of 100 mW cm^{-2} under the simulated one-sun AM 1.5 G solar irradiance in ambient air. The J–V curves were carried out under both forward and reverse scan in the range from 0 to 1.2 V. Scanning electron microscopy (SEM) images were acquired by using a field-emission scanning electron microscope (JEM-4800F). The incident photon-to-electron conversion efficiency (IPCE) was recorded by a computer-controlled IPCE system (Newport). Photoluminescence (PL) (excitation at 470 nm) and the time-resolved photoluminescence (TRPL) decay measurements were prepared using a FLSP920 spectrometer (Edinburgh Instruments LTD). Impedance spectroscopic measurement was carried out using an electrochemical analyzer (Autolab 320, Metrohm, Switzerland) with a constant reverse potential from 0 to 1 V in the dark. The crystal structure of the perovskite thin films was performed by a Rigaku (RINT-2500) X-ray diffraction patterns (Cu Ka radiation, λ = 1.5418 Å).

3. Results and discussion

The schematic device diagram and self-assembled structure of n-DMBI-doped PTEG-1 layer are shown in Fig. 1a, with a structure of FTO/n-DMBI-doped PTEG-1/$CH_3NH_3PbI_3$/Spiro-OMeTAD/Au. The ETL

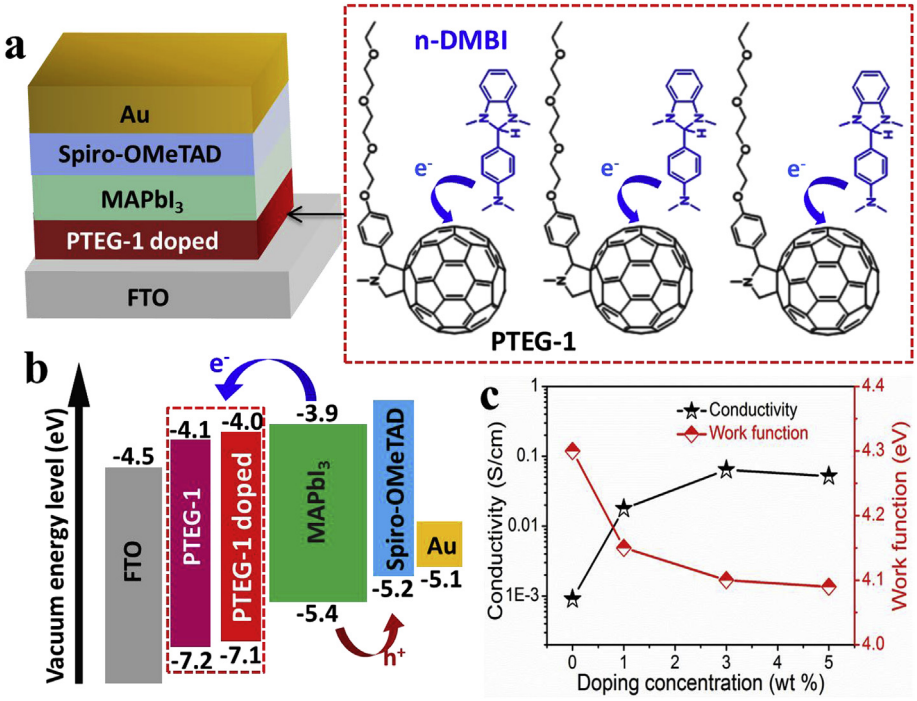

Fig. 1. (a) Schematic of the PSC devices and the n-DMBI-doped PTEG-1 layer molecular self-assembly structure. (b) Energy diagram: LUMO and HOMO energy levels of the ETL based pure PTEG-1 and 3 wt% doped PTEG-1. (c) Conductivity and work function of n-DMBI doped PTEG-1 film at different doping concentration.

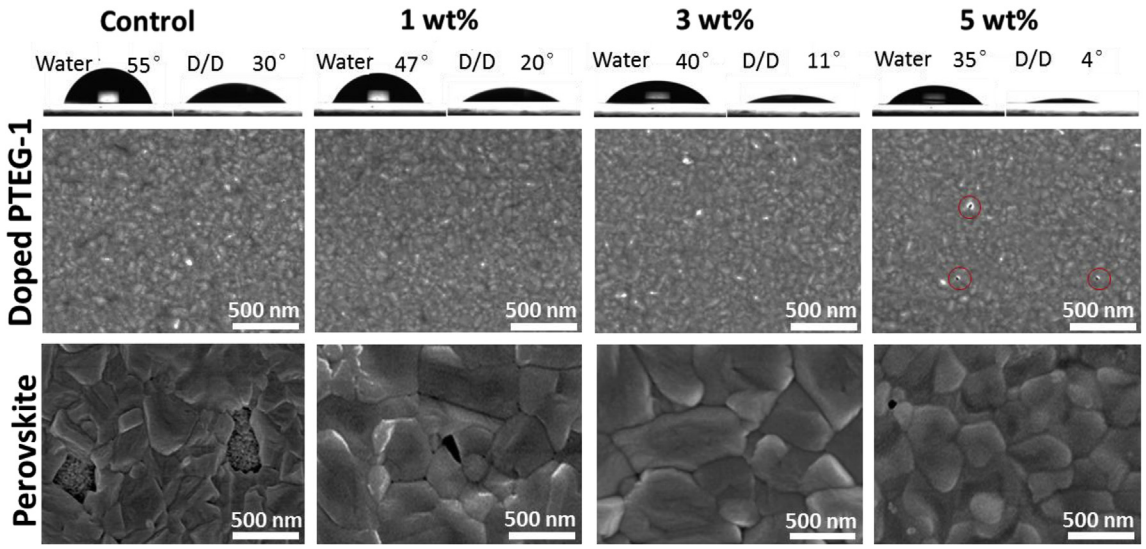

Fig. 2. The images on top show contact angle measurement of water and DMF/DMSO on control and doped PTEG-1 films. The top-view of control and n-DMBI doped PTEG-1 films and perovskite films deposited on control and n-DMBI doped PTEG-1 films. The red circles highlight voids/defects of the PTEG-1 film. (For interpretation of the references to colour in this figure legend, the reader is referred to the Web version of this article.)

is composed of n-DMBI-doped PTEG-1 in the n–i–p planar PSCs. n-DMBI was added into a PTEG-1 solution in a variable dopant concentration (0 wt%, 1 wt%, 3 wt%, 5 wt%). On the one hand, the structural part of n-DMBI is similar to the basic tertiary amine moiety in PTEG-1 molecule. On the other hand, the n-DMBI and PTEG-1 molecules both exists a large polarity [26,27]. These similarities facilitate the miscibility of n-DMBI and PTEG-1 molecules in chlorobenzene solution. Through the introduction of n-DMBI, the vertical orientation of the PTEG-1 molecular arrangement is further improved. In this way, n-DMBI can induce and accelerate efficient electron transport [25]. As demonstrated in Fig. 1c, the n-DMBI dopant can effectively modify the conductivity and work function of PTEG-1 film. The conductivity of the PTEG-1 film almost increased by two orders of magnitude from 9×10^{-4} S/cm of pristine PTEG-1 to 5.2×10^{-2} S/cm of 5wt% n-DMBI-doped PTEG-1. This means the n-DMBI can largely improves the charge transport of PTEG-1 film. In addition, dielectric constant is an important parameter in terms of charge transfer capability. As shown in Fig. S13, the dielectric constant of n-DMBI doped PTEG-1 was gradually decreased from 5.71 to 3.75 with the increase of dopant concentration from 0 to 5 wt%. The decreased dielectric constant is favorable for the charge transfer, consistent with the conductivity data of n-DMBI doped PTEG-1 [28]. Work function of PTEG-1 film with n-DMBI dopant was characterized by ultraviolet photoemission spectroscopy (UPS), which is gradually dropped from 4.3 eV to 4.1 eV as the increase of dopant concentration from 0 to 5 wt%. UPS spectra and absorption spectra were further used to identify the position of the LUMO and the HOMO

Table 1
Parameters of the devices obtained from the J-V curves presented in Fig. S5.

Device	Voc (V)	Jsc (mA/cm^2)	FF (%)	PCE (%)
Control	1.01	21.81	73.50	16.20
1 wt%	1.02	22.20	75.12	17.01
3 wt%	1.04	22.85	78.04	18.50
5 wt%	0.98	19.95	70.01	13.72

energy level with doping (Fig. S1 and Fig. S2). As illustrated from the energy diagram (Fig. 1b), the upshift of LUMO level for doped PTEG-1 is expected to favor the exciton dissociation and electron transport. The LUMO (3.9 eV) of $CH_3NH_3PbI_3$ exhibits a good alignment with that of doped PTEG-1 compared to pure PTEG-1, which indicates favorable electron transport between doped PTEG-1 and $CH_3NH_3PbI_3$ layers. The synergistic effects of the lower work function of doped PTEG-1 and the good energy alignment between perovskite and doped PTEG-1 layers can provide the driving force of effective electron transport from perovskite to PTEG-1. Those results initially confirm the doping effect of n-DMBI in PTEG-1.

Control over the surface morphology is another key issue for high-performance PSCs. Scanning electron microscopy (SEM) and the profile plot were adopted to examine the n-DMBI doping effect towards the morphology of perovskite layer, as shown in Fig. 2. Interestingly, n-DMBI-doped PTEG-1 film exhibited less pinholes and more smooth surface compared to the control sample. Unfortunately, probably due to over-doping related inhomogeneity of host and dopant, 5 wt% n-DMBI doping results in the emergence of vacancies/voids. It is plausible that 5 wt% over-doping leads to the precipitation of n-DMBI dopant out of the self-assembly host-dopant structure.

To further explore the inherent mechanism, surface wettability of N,N-dimethylformamide (DMF)/Dimethyl Sulphoxide (DMSO) (v/v 4:1) and water on pure and doped PTEG-1 film was systematically studied (Fig. 2). The contact angles of DMF/DMSO and water on the PTEG-1 surface gradually decrease with increasing doping concentration, indicating that n-DMBI doping can effectively improve the wettability of the PTEG-1 film. This could be originated from the increased surface tension of PTEG-1 film. Meanwhile, the coverage ratio of $CH_3NH_3PbI_3$ film upon the PTEG-1 layer is increased from 82% to over 96%, due to the improved hydrophilic surface of n-DMBI modification. The perovskite film based on 3wt% doped PTEG-1 exhibits almost full coverage and free vacancies/voids. The improved PTEG-1 wettability can be further confirmed by X-ray diffraction (XRD) characterization (Fig. S4) and the top-view SEM images of the $CH_3NH_3PbI_3$ (Fig. 2). Compared with the control film, the perovskite film based on 3wt% doped the PTEG-1 shows more dense surface with larger crystal grain size. Obviously, under the same experimental conditions, the perovskite film based on the 3 wt% doped PTEG-1 demonstrated the strongest diffraction intensity, indicating that the best crystallinity of $CH_3NH_3PbI_3$ film was achieved (Fig. S4). Reasonably, the peak intensity of the perovskite film based on 5 wt% doped PTEG-1 was dropped and broadened, which resulted in decreased crystallinity of perovskite grains (Fig. S4). In addition, the further improved wettability on the 5 wt% doped PTEG-1 film increased the nucleation site of perovskite, but deviate from the balance between the film coverage and grain size, which can worsen the device performance. These results can be corroborated by reduced perovskite grain size and the presence of vacancies/voids of the perovskite film [29,30].

To examine the practicability of n-DMBI-doped PTEG-1 as ETL in the planar PSCs, devices with architecture of FTO/ETL/$CH_3NH_3PbI_3$/Spiro-OMeTAD/Au were fabricated. The cross-sectional SEM image of as-fabricated PSCs was shown in the Fig. S5b. Accordingly, current density-voltage (J − V) curves of devices with pristine and various doped PTEG-1 films were shown in Fig. S5a. The control device exhibited an impressive PCE of 16.2%, while the highest PCE for similar device structure reported so far was 15.7% from Loi group [23]. The optimized doping concentration of 3 wt% n-DMBI dramatically enhanced the overall device performance in J_{SC} (22.85 mA/cm^2), V_{OC} (1.04 V), FF (78%), and PCE (18.5%), compared to that of the control cell in J_{SC} (21.81 mA/cm^2), V_{OC} (1.01 V), FF (73.5%), and PCE (16.2%). Recently, Snaith group demonstrated that C_{60} with 4-(1,3-dimethyl-2,3-dihydro-1H-benzimidazol-2-yl)-N,N-diphenylaniline (n-DPBI) doping can enhance device efficiency and improve long-term stability at room temperature. However, in order to activate the doping, the spin-coated n-DPBI-doped C_{60} film has to go through thermal annealing for 12 h at 80 °C [19]. In contrast, the preparation of n-DMBI-doped PTEG-1 film doesn't require time-consuming thermal-activation process, and single-step spin-coating procedure without any further annealing can produce high-quality doped PTEG-1 film. Compared with n-DPBI, n-DMBI has an increased electron-donating strength of the amine functionality, easily incorporating in the side chain plane in the case of not disturbing the π–π packing of PTEG-1 [25]. To avoid the experiment accidental errors, statistical distribution of thirty devices fabricated with pure and n-DMBI doped PTEG-1 ETL is shown in the form of a box plot (Fig. S6). The corresponding parameters are listed in Table 1. The J-V characteristics of the best performing devices with pristine and doped PTEG-1 as the ETL are shown in Fig. 3a. A reference device based on $CH_3NH_3PbI_3$ perovskite delivers the performance with PCE of 16.2%, J_{SC} of 21.81 mA/cm^2, V_{OC} of 1.01 V, and FF of 73.5%. Correspondingly, n-DMBI-doped PTEG-1 ETL based device exhibits significant enhancement in both J_{SC}, and FF. Champion device based on the doped PTEG-1 ETL shows outstanding performance with PCE of 18.5%, J_{SC} of 22.85 mA/cm^2, V_{OC} of 1.04 V, and FF of 0.78 (Fig. 3d). The corresponding parameters are listed in Table S1. To further understand the mechanism for the performance enhancement, the IPCE and the integrated current density of the device are shown in Fig. 3b. The curves show a similar tendency but different intensity in accordance with current density difference from n-DMBI doping. The stabilized photocurrent output of the 3 wt% n-DMBI doping based on cell is recorded at a forward bias of 0.846 V. A steady-state PCE of 18.33% is obtained at the maximum power point (Fig. 3e). This result is almost the same as the PCE that is obtained from the J-V curve. Especially, the J-V hysteresis is harmful for the solar harvesting. n-DMBI dopant can effectively alleviate hysteresis as shown in Fig. 3c. Almost non-hysteresis is observed for the PSCs with 3wt% doping PTEG-1. The photovoltaic parameters of the PSCs based on pristine and 3wt% doped PTEG-1 as ETL from short circuit to forward bias (SC-FB) and from forward bias to short circuit (FB-SC) are demonstrated in Table S2. The negligible hysteresis in PSCs based on doped PTEG-1 could be ascribed to large perovskite grains and improved conductivity by n-DMBI [31–33]. PCEs for 30 cells using pristine PTEG-1 or the 3 wt% doped PTEG-1 as ETL was recorded. The PCE histograms of the cells are shown in Fig. 3f, indicating cells based on doped PTEG-1 are highly reproducible with a small variation.

Generally, the enhancement in J_{SC} with n-DMBI doped PTEG-1 ETL could be attributed to excellent charge transport, high conductivity/mobility, and well energy-band alignment. As expected, the FF for the doped PTEG-1 devices is higher than that of control cells, due to the reduced series resistance of the doped PTEG-1 cells. Electrochemical impedance spectroscopy (EIS) was conducted to further invesitgate carrier transport behavior at the interfaces of doped PTEG-1/$MAPbI_3$/spiro-OMeTAD. We found that the addition of n-DMBI dopant increased recombination resistance and decreased interfacial recombination rate (Fig. S7 and Table S4). The device with the doped PTEG-1 ETL also showed a slightly increased in V_{OC} compared to the reference cell. This may result from the reduced trap-state and the defects around interface of ETL and perovskite. The combined effects of the obtained trends in V_{OC}, FF and J_{SC} can be observed in Fig. S6, which reveals the PCE distribution for different device conditions. The optimized PCE from devices based on $CH_3NH_3PbI_3$ perovskite with pure and doped PTEG-1 as ETL is consistent with the above analysis.

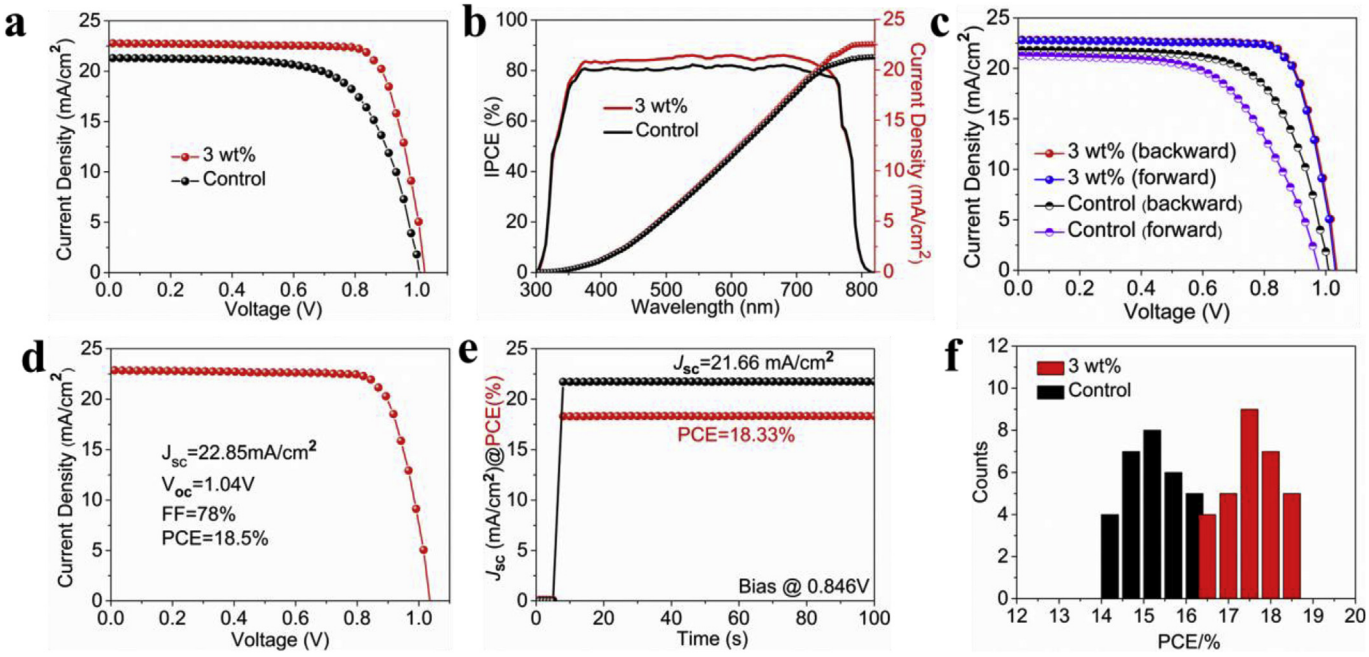

Fig. 3. (a) and (d) The J – V curve of the control and n-DMBI-doped PTEG-1 based devices. (b) The IPCE spectra and the integrated J_{SC} of the control and n-DMBI doped PTEG-1 based devices. (e) Steady-state efficiency with the photocurrent density of the best PSC with 3 wt% doped PTEG-1. (c) The J-V curves (different scanning directions) and (f) PCE distribution of the devices based control and 3 wt% doped PTEG-1 films.

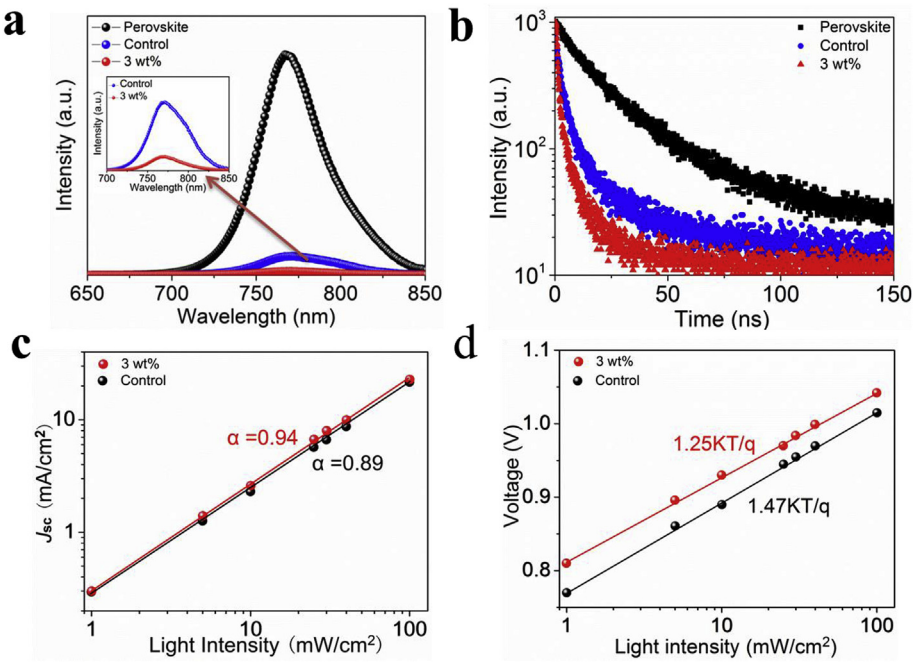

Fig. 4. (a) Steady-state and (b) Time-resolved photoluminescence (PL) spectra of perovskite deposited on control and 3 wt% doped coated glass/FTO substrates; Light intensity dependence of control and 3 wt % doped perovskite solar cells with (c) Jsc versus light intensity and (d) Voc versus light intensity. The inset in (a) is a magnifcation of steady-state PL spectra.

To further explore the reason of performance enhancement in the $CH_3NH_3PbI_3$ PSCs, steady state photoluminescence (PL) and time-resolved photoluminescence (TRPL) spectra were used to investigate n-DMBI doping effect on photogenerated carrier extraction from perovskite absorber to PTEG-1 ETL. The PL spectra of the corresponding three samples: glass/FTO/perovskite, glass/FTO/PTEG-1/perovskite, and glass/FTO/PTEG-1 doped/perovskite, are shown in Fig. 4a. The $CH_3NH_3PbI_3$ perovskite film deposited on 3 wt% n-DMBI-doped PTEG-1 shows a significant PL quenching effect, compared to the undoped PTEG-1 film, which proves that the n-DMBI dopant can largely enhance the rate of electron extraction and may decrease carrier recombination at the ETL/perovskite interface [34,35]. The TRPL decay spectra of the perovskite films deposited on pure or doped PTEG-1 ETL were measured. Transient PL curves for perovskite films on glass/FTO, glass/FTO/pure PTEG-1, and glass/FTO/doped PTEG-1 are plotted in Fig. 4b. The detailed fitting parameters are summarized in Table S3. Apparently, it shows a much faster PL decay for 3 wt% n-DMBI-doped PTEG-1, compared to the pure PTEG-1 sample. The addition of n-DMBI dopant effectively decreases non-radiative recombination at the perovskite/ETL interface through reducing density of trap-state and the defects, leading to a large increase in J_{SC}. Those findings are consistent with the results from EIS [36–38]. The addition of the n-DMBI dopant decreases the charge-transfer resistance and the ohmic resistance (Fig. S7). Thus, PL, TRPL, and EIS investigations confirmed that 3 wt% n-

DMBI dopant can largely facilitate carrier transfer and suppress charge recombination from perovskite to PTEG-1 layer. These results are consistent with the higher J_{SC}, V_{OC} and FF in the n-DMBI doped PSCs.

Fig. 4c shows the power law dependence of J_{SC} versus light intensity ($J \propto I^{\alpha}$). The value of α expresses the extent of space charge effect. A cell with α value close to 1 or 0.75 means the device is without or with space charge effect, respectively [39]. The doped PTEG-1 devices have a higher α value, which further confirmed that more excited electrons are effectively captured by electrodes before recombination, compared to the control device. Fig. 4d demonstrated light intensity dependence of V_{OC} of pristine and doped PTEG-1 devices at room temperature (≈300 K). This curve could identify the recombination mechanism of photogenerated charge carrier when light intensity changed. The experimental slopes (n), where n = 2 or 1 represent the extreme dominant cases of Shockley–Read–Hall nonradiative (monomolecular) or radiative (bimolecular) recombination, respectively, are equal to kT/q for all devices without trap-assisted carrier recombination within experimental error [40]. The device using pristine PTEG-1 as the ETL shows a slope of 1.47kT/q, indicating a significant nonradiative trap-assisted recombination. After doping n-DMBI into PTEG-1, the slope is decreased to 1.25kT/q, indicative of the dominance of radiative defect-assisted recombination in devices, which is in consistent with the decrease of the nonradiative trap-assisted recombination [41]. Consequently, the doped PTEG-1 restrains the trap-assisted recombination more effectively than pristine PTEG-1. Moreover, the relationship of J_{SC}/V_{OC} versus light intensity manifested reduced surface trap-state and defects for devices based on n-DMBI doped PTEG-1, favoring faster charge separation at the perovskite/PTEG-1 interface. These results comply with PL/TRPL/EIS study and further imply the origin of performance enhancement.

Long-term stability (> 1000 h) remains a significant challenge before the commercialization of PCSs. Especially, few studies are focusing on the stability investigation of PSCs at high temperature (≥60 °C) [42,43]. Here, long-term thermal stability of doped/undoped PTEG-1 and TiO_2 based PCSs was comparatively investigated. All unsealed devices were tested for 1000 h at 60 °C with the humidity of 20%. The J-V curves of TiO_2-based PSCs are demonstrated in Fig. S8, which are n-i-p architecture similar as our previous work [44]. The $CH_3NH_3PbI_3$ film deposited on doped PTEG-1 substrate demonstrated two times larger crystal grain in diameter (Fig. S9) and maintained tetragonal structure after 1000 h at 60 °C (Fig. S10), compared with that deposited on TiO_2, which may be reasons for the improvement of PETG-1-based PCSs in performance and thermal-stability. In Fig. 5, normalized PCE, J_{SC}, V_{OC} and FF were depicted independently against storage time to provide a better view on thermal stability among the three types of devices. As expected, all performance parameters of TiO_2-based PSCs drastically dropped by over 75% from its original best value after 500 h, which is the characteristics of perovskite degradation. The impurity new peak at 12.7° in XRD pattern (Fig. S10) can be identified as the existence of PbI_2, referring to the collapse of crystallized $CH_3NH_3PbI_3$ [45]. The accelerated decomposition of $CH_3NH_3PbI_3$ is induced by thermal activated photocatalytic properties of TiO_2. After 120 h continuous full spectral illumination, XRD pattern of perovskite film deposited on TiO_2 ETL displayed a new peak at 12.7°, associated with PbI_2 impurity (Fig. S11). This implies UV-light photocatalysis of TiO_2 can lead to the decomposition of $CH_3NH_3PbI_3$ film. In contrast, the perovskite films deposited on n-DMBI-doped PTEG-1 ETL exhibited both strong thermal stability and photostability. The XRD patterns of perovskite films demonstrated pure $CH_3NH_3PbI_3$ crystal structure without any impurity peak after long-term storage at high temperature or under light illumination (Fig. S10 and Fig. S11). The PCE of pristine PTEG-1 based PSCs retained 45% of the initial PCE after 500 h and then decreased to a stabilized 39% of its highest record after 600 h storage at 60 °C, much more stable than that of TiO_2-based PCSs. This improvement may be ascribed to the chemical structure of PTEG-1, whose side chains of the triethylene oxide moieties and tertiary amine can tightly bond with the iodide vacancies and thus effectively suppress the trap-assisted recombination. Strikingly, the doped PTEG-1 cell kept 85% of the initial PCE after 1000 h storage at 60 °C, which proved that the introduction of n-DMBI significantly increased the thermal stability of cells compared to the control and TiO_2 based cells. In addition, V_{OC} and FF of the device with doped PTEG-1 retained over 90% of the original highest value after 1000 h. Meanwhile, long-term thermal stability of unencapsulated doped/undoped PTEG-1 and TiO_2 based PCSs was also tested for 500 h at 85 °C with the humidity of 20%. The corresponding results were shown in Fig. S12. It was found that the PCE of TiO_2-based PSCs decreased to 15% of the initial highest record after 300 h storage at 85 °C. The pure PTEG-1 cell kept 35% of the initial PCE after 500 h storage at the same temperature. The doped PTEG-1 cell exhibited the strongest thermal stability among the three types of cells, retaining 65% of the initial PCE after 500 h storage at 85 °C. These results imply a perfect and stable interface between n-DMBI-doped PTEG-1 and perovskite layers. Interestingly, after 1000 h, J_{SC} of the n-DMBI-doped PCSs decreased to 80% of its initial value at 60 °C, which may be mainly responsible for the decay in PCE. It is plausible that the drop of J_{SC} should primarily be attributed to the diffusion of metal into Spiro-OMeTAD layer at high temperature [43]. These results demonstrate that the PSCs based on n-DMBI-doped PTEG-1 film possess an outstanding long-term thermal stability, compared to pristine PTEG-1 or TiO_2 based PSCs. Meanwhile, we summarized the thermal stability parameters of PSCs from other reported works in Table S5. It is found that the cells based on our doped fullerene derivatives exhibited excellent thermal stability. We believe that there exist several factors leading to the enhanced thermal stability:

(1) Except that strong coordinating capability of PTEG-1 itself with $CH_3NH_3PbI_3$ induced effective suppression on trap-assisted recombination in PSCs, the self-assembly n-DMBI-doped PTEG-1 film has achieved a firm well-oriented nanostructure as shown in the inset of Fig. 1. Typically, different from any previous reported work, this dopant/host nanostructure can be readily formed after solution-processing without any further annealing. Without disturbing the π–π structure of PTEG-1, the polarized n-DMBI molecules with basic tertiary amine moiety can be inserted between the C_{60} contained planes, and coupled orderly with the triethylene glycol type side chain of PTEG-1 (inset of Fig. 1a) [24]. Hence, by introducing n-DMBI dopant, more stable PTEG-1 matrix, more conductive ETL, and more hydrophilic surface could be achieved. All these improvements are beneficial for perfect ETL/perovskite interface and thus long-term thermal stability of PSCs.
(2) We mainly attributed the ~15% PCE decay of device with doped PTEG-1 to the instable interface of Au/Spiro-OMeTAD and Spiro-OMeTAD/perovskite. The metal diffusion into Spiro-OMeTAD layer at high temperature results in device degradation [46]. Additionally, high-quality Spiro-OMeTAD layer seriously relies on the additives of LiTFSI, 4-tert-butylpyridine, and Co (III) p-dopant complex. These additives can easily migrate within the whole device at 60 °C, negatively affecting the long-term device stability [47,48]. Interfacial layers [49,50] or alternative inorganic hole transport materials [51] have been introduced to achieve long-term thermal stable PCSs.

4. Conclusions

In summary, a promising n-doped fullerene derivative system was applied as an effective ETL for the planar-heterojunction n-i-p PSCs, which was prepared by room-temperature solution process without additional annealing. The n-DMBI dopant increases the conductivity and reduces the work function of the PTEG-1 film. Meanwhile, the n-DMBI dopant can tune the surface wettability of the PTEG-1 film, which favors the formation of dense and stable perovskite film. Through PL, TRPL and EIS characterizations, it is confirmed that n-DMBI dopant can

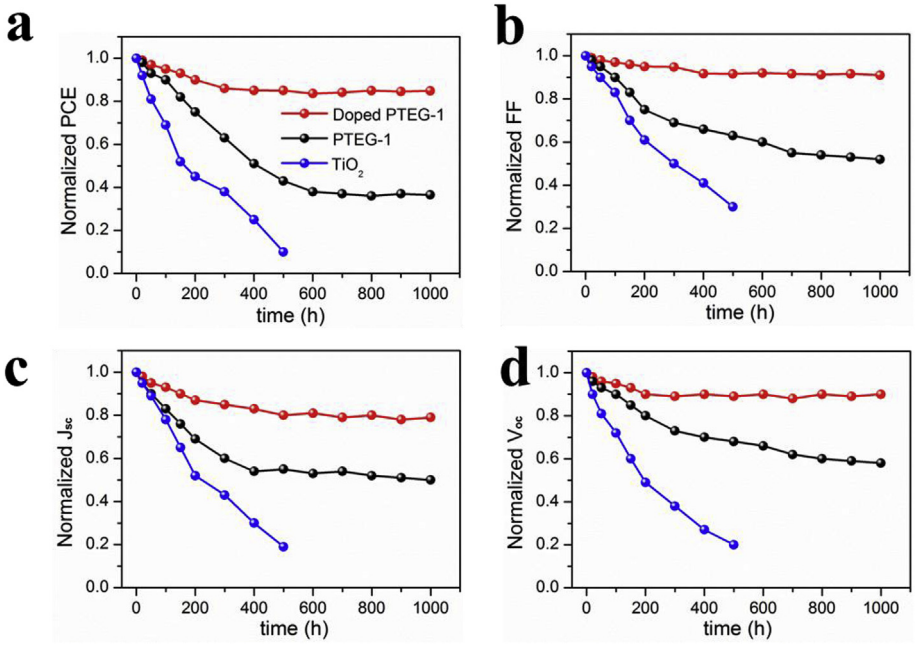

Fig. 5. The normalized PCE (a); FF (b); Jsc (c); Voc (d) change of the devices with the different ETLs kept in air at 60 °C with the humidity of 20%.

largely facilitate carrier transfer and suppress charge recombination from perovskite to PTEG-1 layer. Thanks to these progresses, a high J_{SC} in excess of 22.8 mA/cm^2, and FF of 78% were obtained by optimizing the doping ratio of n-DMBI dopant. The PCE of PSCs using doped PTEG-1 (18.5%) can outperform the ones based on pristine PTEG-1 or the other fullerene derivatives such as PCBM. More importantly, un-encapsulated PSCs based on this doped PTEG-1 exhibited negligible J–V hysteresis and led to remarkable long-term thermal stability under ambient conditions. The doped PTEG-1 cells kept 85% of the initial PCE over 40-days storage at 60 °C with the humidity of 20%. Our high-efficiency device, along with the outstanding thermal stability demonstrated by the PSCs based on n-doped fullerene derivative, should be beneficial for their commercial deployment.

Acknowledgement

The authors acknowledge the financial support by the National Nature Science Foundation of China (51473172, 51473173, 21401167, 21203209, 21301180, 21671193 and 21303218), the National Key R& D Program of China (Grant Nos. 2018YFA0208501, 2016YFB0401603, 2016YFC1100502 and 2016YFB0401100), the Fundamental and Advanced Technology Research Program from the Science and Technology Department of Henan Province (142300410031.0), and the Science and Technology Key Project from the Education Department of Henan Province (Grant No. 14A510001).

Appendix A. Supplementary data

Supplementary data related to this article can be found at https://doi.org/10.1016/j.jpowsour.2018.12.066.

UPS and absorption spectra of doped PTEG-1 films. The X-ray diffraction patterns of perovskite films. The J − V curves of devices. Nyquist plots of the cells.

References

[1] M.M. Lee, J. Teuscher, T. Miyasaka, T.N. Murakami, H.J. Snaith, Efficient hybrid solar cells based on meso-superstructured organometal halide perovskites, Science 338 (2012) 643.

[2] G. Xing, N. Mathews, S. Sun, S.S. Lim, Y.M. Lam, M. Grätzel, S. Mhaisalkar, T.C. Sum, Long-range balanced electron-and hole-transport lengths in organic-inorganic $CH_3NH_3PbI_3$, Science 342 (2013) 344–347.

[3] S.D. Stranks, G.E. Eperon, G. Grancini, C. Menelaou, M.J. Alcocer, T. Leijtens, L.M. Herz, A. Petrozza, H.J. Snaith, Electron-hole diffusion lengths exceeding 1 micrometer in an organometal trihalide perovskite absorber, Science 342 (2013) 341–344.

[4] A. Kojima, K. Teshima, Y. Shirai, T. Miyasaka, Organometal halide perovskites as visible-light sensitizers for photovoltaic cells, J. Am. Chem. Soc. 131 (2009) 6050–6051.

[5] W.S. Yang, B.W. Park, E.H. Jung, N.J. Jeon, Y.C. Kim, D.U. Lee, S.S. Shin, J. Seo, E.K. Kim, J.H. Noh, S.N. Seok, Iodide management in formamidinium-lead-halide-based perovskite layers for efficient solar cells, Science 356 (2017) 1376–1379.

[6] M.A. Green, K. Emery, Y. Hishikawa, W. Warta, E.D. Dunlop, Solar cell efficiency tables (version 48), Prog. Photovoltaics Res. Appl. 7 (2016) 905–913.

[7] Y. Zhang, X. Liu, P. Li, Y. Duan, X. Hu, F. Li, Y. Song, Dopamine-crosslinked TiO_2/perovskite layer for efficient and photostable perovskite solar cells under full spectral continuous illumination, Nano Energy 56 (2019) 733–740.

[8] J. Cao, B. Wu, R. Chen, Y. Wu, Y. Hui, B.-W. Mao, N. Zheng, Efficient, hysteresis-free, and stable perovskite solar cells with ZnO as electron-transport layer: effect of surface passivation, Adv. Mater. 30 (2018) 1705596.

[9] H. Gu, C. Zhao, Y. Zhang, G. Shao, Stable high-performance perovskite solar cells based on inorganic electron transporting bi-layers, Nanotechnology 29 (2018) 385401.

[10] Y.C. Kim, T.Y. Yang, N.J. Jeon, J. Im, S. Jang, T.J. Shin, H.-W. Shin, S. Kim, E. Lee, S. Kim, J.H. Noh, S.I. Seok, J. Seo, Engineering interface structures between lead halide perovskite and copper phthalocyanine for efficient and stable perovskite solar cells, Energy Environ. Sci. 10 (2017) 2109–2116.

[11] H. Tan, A. Jain, O. Voznyy, X. Lan, F.P.G. de Arquer, J.Z. Fan, R. Quintero-Bermudez, M. Yuan, B. Zhang, Y. Zhao, F. Fan, P. Li, L.N. Quan, Y. Zhao, Z.-H. Lu, Z. Yang, S. Hoogland, E.H. Sargent, Efficient and stable solution-processed planar perovskite solar cells via contact passivation, Science 355 (2017) 722–726.

[12] Q. Lin, A. Armin, R.C.R. Nagiri, P.L. Burn, P. Meredith, Electro-optics of perovskite solar cells, Nat. Photon. 9 (2015) 106–112.

[13] O. Malinkiewicz, A. Yella, Y.H. Lee, G.M. Espallargas, M. Grätzel, M.K. Nazeeruddin, H.J. Bolink, Perovskite solar cells employing organic charge-transport layers, Nat. Photon. 8 (2014) 128–132.

[14] J.Y. Jeng, Y.F. Chiang, M.H. Lee, S.R. Peng, T.F. Guo, P. Chen, T.C. Wen, $CH_3NH_3PbI_3$ perovskite/fullerene planar-heterojunction hybrid solar cell, Adv. Mater. 25 (2013) 3727–3732.

[15] F. Zhang, W. Shi, J. Luo, N. Pellet, C. Yi, X. Li, X. Zhao, T.J.S. Dennis, X. Li, S. Wang, Y. Xiao, S.M. Zakeeruddin, D. Bi, M. Grätzel, Isomer-pure bis-PCBM-assisted crystal engineering of perovskite solar cells showing excellent efficiency and stability, Adv. Mater. 29 (2017) 1606806.

[16] J. Xie, V. Arivazhagan, K. Xiao, K. Yan, Z. Yang, Y. Qiang, P. Hang, G. Li, C. Cui, X. Yu, D. Yang, A ternary organic electron transport layer for efficient and photo-stable perovskite solar cells under full spectrum illumination, J. Mater. Chem. 6 (2018) 5566–5573.

[17] J. You, Z. Hong, Y.M. Yang, Q. Chen, M. Cai, T.B. Song, C.C. Chen, S. Lu, Y. Liu, H. Zhou, Y. Yang, Low-temperature solution-processed perovskite solar cells with high efficiency and flexibility, ACS Nano 8 (2014) 1674–1680.

[18] C. Kuang, G. Tang, T. Jiu, H. Yang, H. Liu, B. Li, W. Luo, X. Li, W. Zhang, F. Lu, J. Fang, Y. Li, Highly efficient electron transport obtained by doping PCBM with graphdiyne in planar-heterojunction perovskite solar cells, Nano Lett. 15 (2015)

2756–2762.
[19] Z. Wang, D.P. McMeekin, N. Sakai, S. Reenen, K. Wojciechowski, J.B. Patel, M.B. Johnston, H.J. Snaith, Efficient and air-stable mixed-cation lead mixed-halide perovskite solar cells with n-doped organic electron extraction layers, Adv. Mater. 29 (2017) 1604186.
[20] Q. Liu, J. Toudert, F. Liu, P. Mantilla-Perez, M.M. Bajo, T.P. Russell, J. Martorell, Circumventing UV light Induced nanomorphology disorder to achieve long lifetime PTB7-Th: PCBM based solar cells, Adv. Energy Mater. 7 (2017) 1701201.
[21] F. Xia, Q. Wu, P. Zhou, Y. Li, X. Chen, Q. Liu, J. Zhu, S. Dai, Y. Lu, S. Yang, Efficiency enhancement of inverted structure perovskite solar cells via oleamide doping of PCBM electron transport layer, ACS Appl. Mater. Interfaces 7 (2015) 13659–13665.
[22] P. Li, C. Liang, Y. Zhang, F. Li, Y. Song, G. Shao, Polyethyleneimine high-energy hydrophilic surface interfacial treatment toward efficient and stable perovskite solar cells, ACS Appl. Mater. Interfaces 8 (2016) 32574–32580.
[23] S. Shao, M. Abdu-Aguye, L. Qiu, L.H. Lai, J. Liu, S. Adjokatse, F. Jahani, M.E. Kamminga, G.H. Brink, T.T.M. Palstra, B.J. Kooi, J.C. Hummelenab, M.A. Loi, Elimination of the light soaking effect and performance enhancement in perovskite solar cells using a fullerene derivative, Energy Environ. Sci. 9 (2016) 2444–2452.
[24] P. Wei, J.H. Oh, G. Dong, Z. Bao, Use of a 1 H-benzoimidazole derivative as an n-type dopant and to enable air-stable solution-processed n-channel organic thin-film transistors, J. Am. Chem. Soc. 132 (2010) 8852–8853.
[25] J. Liu, L. Qiu, G. Portale, M. Koopmans, G. Brink, J.C. Hummelen, L. Koster, N-Type Organic thermoelectrics: improved power factor by tailoring host-dopant miscibility, Adv. Mater. 29 (2017) 1701641.
[26] B.D. Naab, S. Guo, S. Olthof, E.G. Evans, P. Wei, G.L. Millhauser, A. Kahn, S. Barlow, S.R. Marder, Z. Bao, Mechanistic study on the solution-phase n-doping of 1,3-Dimethyl-2-aryl-2,3-dihydro-1H-benzoimidazole derivatives, J. Am. Chem. Soc. 135 (2013) 15018–15025.
[27] A. Giovannitti, C.B. Nielsen, D.T. Sbircea, S. Inal, M. Donahue, M.R. Niazi, D.A. Hanifi, A. Amassian, G.G. Malliaras, J. Rivnay, I. McCulloch, N-type organic electrochemical transistors with stability in water, Nat. Commun. 7 (2016) 13066.
[28] F. Jahani, S. Torabi, R.C. Chiechi, L.J.A. Koster, J.C. Hummelen, Fullerene derivatives with increased dielectric constants, Chem. Commun. 50 (2014) 10645–10647.
[29] Y. Ma, Y. Liu, I. Shin, I.W. Hwang, Y.K. Jung, J.H. Jeong, S.H. Park, K.H. Kim, Understanding and tailoring grain growth of lead-halide perovskite for solar cell application, ACS Appl. Mater. Interfaces 9 (2017) 33925–33933.
[30] Q. Qin, Z. Zhang, Y. Cai, Y. Zhou, H. Liu, X. Lu, X. Gao, L. Shui, S. Wu, J. Liu, Improving the performance of low-temperature planar perovskite solar cells by adding functional fullerene end-capped polyethylene glycol derivatives, J. Power Sources 396 (2018) 49–56.
[31] M. Long, T. Zhang, W. Xu, X. Zeng, F. Xie, Q. Li, Z. Chen, F. Zhou, K.S. Wong, K. Yan, J. Xu, Large-grain formamidinium $PbI_{3-x}Br_x$ for high-performance perovskite solar cells via intermediate halide exchange, Adv. Energy Mater. 7 (2017) 1601882.
[32] W. Nie, H. Tsai, R. Asadpour, J.-C. Blancon, A.J. Neukirch, G. Gupta, J.J. Crochet, M. Chhowalla, S. Tretiak, M.A. Alam, H.-L. Wang, A.D. Mohite, High-efficiency solution-processed perovskite solar cells with millimeter-scale grains, Science 347 (2015) 522–525.
[33] P. Li, C. Liang, B. Bao, Y. Li, X. Hu, Y. Wang, Y. Zhang, F. Li, G. Shao, Y. Song, Inkjet manipulated homogeneous large size perovskite grains for efficient and large-area perovskite solar cells, Nano Energy 46 (2018) 203–211.
[34] K. Wang, C. Liu, P. Du, J. Zheng, X. Gong, Bulk heterojunction perovskite hybrid solar cells with large fill factor, Energy Environ. Sci. 8 (2015) 1245–1255.
[35] W. Tress, Perovskite solar cells on the way to their radiative efficiency limit-insights into a success story of high open-circuit voltage and low recombination, Adv. Energy Mater. 7 (2017) 1602358.
[36] C. Wang, Y. Li, C. Zhang, L. Shi, S. Tong, B. Guo, J. Zhang, J. He, Y. Gao, C. Su, J. Yang, Enhancing the performance of planar heterojunction perovskite solar cells using stable semiquinone and amine radical modified hole transport layer, J. Power Sources 390 (2018) 134–141.
[37] A. Dualeh, T. Moehl, N. Tétreault, J. Teuscher, P. Gao, M.K. Nazeeruddin, M. Grätzel, Impedance spectroscopic analysis of lead iodide perovskite-sensitized solid-state solar cells, ACS Nano 8 (2013) 362–373.
[38] R.S. Sanchez, V. Gonzalez-Pedro, J.W. Lee, N.G. Park, Y.S. Kang, I. Mora-Sero, J. Bisquert, Slow dynamic processes in lead halide perovskite solar cells. characteristic times and hysteresis, J. Phys. Chem. Lett. 5 (2014) 2357–2363.
[39] L.J.A. Koster, V.D. Mihailetchi, H. Xie, P.W.M. Blom, Origin of the light intensity dependence of the short-circuit current of polymer/fullerene solar cells, Appl. Phys. Lett. 87 (2005) 203502.
[40] T. Singh, T. Miyasaka, Stabilizing the efficiency beyond 20% with a mixed cation perovskite solar cell fabricated in ambient air under controlled humidity, Adv. Energy Mater. 8 (2018) 1700677.
[41] S.R. Cowan, A. Roy, A. Heeger, Recombination in polymer-fullerene bulk heterojunction solar cells, J. Phys. Rev. B 82 (2010) 245207.
[42] Y. Han, S. Meyer, Y. Dkhissi, K. Weber, J.M. Pringle, U. Bach, L. Spiccia, Y.B. Cheng, Degradation observations of encapsulated planar $CH_3NH_3PbI_3$ perovskite solar cells at high temperatures and humidity, J. Mater. Chem. 3 (2015) 8139–8147.
[43] N. Arora, M.I. Dar, A. Hinderhofer, N. Pellet, F. Schreiber, S.M. Zakeeruddin, M. Grätzel, Perovskite solar cells with CuSCN hole extraction layers yield stabilized efficiencies greater than 20%, Science 358 (2017) 768–771.
[44] C. Liang, P. Li, Y. Zhang, H. Gu, Q. Cai, X. Liu, J. Wang, H. Wen, G. Shao, Mild solution-processed metal-doped TiO_2 compact layers for hysteresis-less and performance-enhanced perovskite solar cells, J. Power Sources 372 (2017) 235–244.
[45] C. Wang, C. Zhang, S. Wang, G. Liu, H. Xia, S. Tong, J. He, D. Niu, C. Zhou, K. Ding, Y. Gao, J. Yang, Low-temperature processed, efficient, and highly reproducible cesium-doped triple cation perovskite planar heterojunction solar cells, Solar RRL, vol. 2, 2018, p. 1700209.
[46] Y. Han, S. Meyer, Y. Dkhissi, K. Weber, J.M. Pringle, U. Bach, L. Spiccia, Y.-B. Cheng, Degradation observations of encapsulated planar $CH_3NH_3PbI_3$ perovskite solar cells at high temperatures and humidity, J. Mater. Chem. 3 (2015) 8139–8147.
[47] F. Bella, G. Griffini, J.-P. Correa-Baena, G. Saracco, M. Grätzel, A. Hagfeldt, S. Turri, C. Gerbaldi, Improving efficiency and stability of perovskite solar cells with photocurable fluoropolymers, Science 354 (2016) 203–206.
[48] Y. Xue, Y. Wu, Y. Li, Readily synthesized dopant-free hole transport materials with phenol core for stabilized mixed perovskite solar cells, J. Power Sources 344 (2017) 160–169.
[49] L. Liu, P. Su, H. Yao, J. Wang, W. Fu, X. Liu, H. Yang, Optimized interface and recrystallized grains by CsBr treatment for enhanced photovoltaic performance of perovskite solar cells, J. Power Sources 389 (2018) 50–55.
[50] H. Kim, K.G. Lim, T.W. Lee, Planar heterojunction organometal halide perovskite solar cells: roles of interfacial layers, Energy Environ. Sci. 9 (2016) 12–30.
[51] S.B. Mane, A.A. Sutanto, C.F. Cheng, M.Y. Xie, C.I. Chen, M. Leonardus, S.-C. Yeh, B.B. Beyene, E.W.-G. Diau, C.-T. Chen, C.H. Hung, Oxasmaragdyrins as new and efficient hole-transporting materials for high-performance perovskite solar cells, ACS Appl. Mater. Interfaces 9 (2017) 31950–31958.